

University of Birmingham

School of Engineering  
Department of Mechanical Engineering

## Advanced Manufacturing Individual Report

### Investigation of Nanosecond laser Pulse on Stainless Steel 316 Using the Finite Difference Method

Name	Alexander Dawes
ID number	2206650
Professors	Prof. Khamis Essa, Prof. Stefan Dimov

#### Symbols

Table 1- Symbol Definition

$\rho$	Density ( $\frac{kg}{m^3}$ )
$Cp$	Specific Heat Capacity ( $\frac{J}{kgK}$ )
$k$	Thermal Conductivity ( $\frac{W}{mK}$ )
$P_{av}$	Average Power ( $W$ )
$f$	Repetition Frequency ( $Hz$ )
$\tau$	Pulse Duration ( $s$ )
$R$	Beam Spot Radius ( $m$ )
$\alpha$	Absorption Co-efficient ( $m^{-1}$ )
$Lm$	Latent Heat of Melting ( $\frac{kJ}{kg}$ )

## Introduction

Nanosecond range lasers are commonly used in many fields of research and manufacture, such as subtractive laser machining [1] and additive manufacturing technologies such as laser powder bed fusion.[2] Subtractive laser machining is a commonly used manufacturing technique that can selectively remove material from a workpiece via laser ablation of material. Ablation is the removal of material via instantaneous evaporation of the material without phase change to liquid. [3] The amount of material removed is directly related to the depth of the crater formed from the incident laser pulse. This paper investigates the simulation of an individual nanosecond range laser pulse on a 2-D flat rectangular substrate of stainless steel 316 using the finite difference method. The main aims were to determine the depth of the ablated crater for specified laser parameters and to investigate the different thermal effects present. Nanosecond range lasers are in the thermal processing range of laser pulse times [3], so there were notable thermal effects such as a melt zone and a heat affected zone. A parallel experiment was conducted in order to validate the model based on the depth of the ablated crater. The simulation was found to be within 14% of experimental result.

## Methodology

The simulation of an individual laser pulse on a material requires the underlying mathematical equations to be solved through time to determine the temperatures throughout the pulse. The standard heat conduction equation with a volumetric heat source gaussian laser pulse was selected to model the system. Convection and radiation were omitted from the equation. The standard heat equation with laser pulse can be written as:

$$\rho C_p \frac{\delta T(x, z, t)}{\delta t} = k \left( \frac{\delta^2 T}{\delta x^2} + \frac{\delta^2 T}{\delta z^2} \right) + A(x, z, t) \quad \text{Eq. 1}$$

Where the first term represents the change of temperature with respect to time. The second term represents the conduction in the material, causing change in temperature in both x and z directions. The third term represents the Laser pulse, it is a function of both directions and time and can be modelled via:

$$A(x, z, t) = \alpha * \frac{P_{av}}{f \tau \pi R^2} * \exp \left( -2 \left( \frac{x}{R} \right)^2 - 2 \left( \frac{t}{\tau} \right)^2 - \alpha z \right) \quad \text{Eq. 2}$$

This requires information such as the average power, repetition frequency, Beam Spot radius, pulse duration, the position in x and z directions and the time. Eq.2 captures the gaussian distribution of the laser in the direction perpendicular to the direction of the laser travel (X-direction). And models the temporal distribution of the laser pulse as a gaussian function. This is a simplification as the tail of the laser pulse has been shown to be longer for similar pulse ranges [4]. Laser penetration into the material (Z-direction) is a function related to the absorption co-efficient,  $\alpha$ , which is the inverse of the optical penetration depth into the material. This is related to the wavelength of the laser, the material being illuminated, and its temperature. [5] This was modelled as a constant for this simulation. Another simplification as thermal effects occur in the material changing the temperature and therefore absorption co-efficient.

To use these equations in an explicit computer-based simulation the finite difference method was applied. Firstly, the substrate was discretised into a structured set of nodes with a fixed difference between them in the x and z directions. This spanned a 2-D space 400 microns wide and 80 microns deep. Then the generic equation for a node was formulated using the forward difference method for

first order terms and the central distance method for second order terms on Eq. 1 This results in the following equation (Eq. 3) for a generic node.

$$\rho Cp \left( \frac{T_{i,j}^{k+1} - T_{i,j}^k}{\Delta t} \right) = k \left( \left( \frac{T_{i+1,j}^k - 2T_{i,j}^k + T_{i-1,j}^k}{\Delta x^2} \right) + \left( \frac{T_{i,j+1}^k - 2T_{i,j}^k + T_{i,j-1}^k}{\Delta z^2} \right) \right) + A(x, z, t) \quad \text{Eq. 3}$$

Where i and j denote the x and z directions respectively and k represents the time. E.G. a term with k+1 represents the value of that term at the next time increment. This can be re-arranged to form the generic expression (Eq. 4) that determines the temperature of a node at position i,j at time k+1. This is of key use in the formation of this explicit method.

$$T_{i,j}^{k+1} = T_{i,j}^k + \frac{\Delta t k}{\rho Cp} \left( \left( \frac{T_{i+1,j}^k - 2T_{i,j}^k + T_{i-1,j}^k}{\Delta x^2} \right) + \left( \frac{T_{i,j+1}^k - 2T_{i,j}^k + T_{i,j-1}^k}{\Delta z^2} \right) \right) + \frac{\Delta t}{\rho Cp} A(x, z, t) \quad \text{Eq. 4}$$

Hence the temperature of a node at the next time increment can be determined using information about the previous timestep and the laser heating term. Given the aforementioned laser pulse governing values, Eq. 4 can be implemented mathematically on MATLAB. However, to ensure the stability of this explicit numerical method, the value of the time increment was taken to be:

$$\Delta t = 0.05 * \frac{\rho Cp \Delta x^2 \Delta z^2}{k(\Delta x^2 + \Delta z^2)} \quad \text{Eq. 5}$$

With these equations, the model is ready to be formulated. However, boundary and initial conditions must be given to solve the model. The Boundary and initial conditions were implemented as follows:

- All nodes were initially set to 293 K.
- Initial time set to 0 ns.
- Nodes at the lower boundary were fixed at 293 K.
- Nodes at the left and right boundary were fixed at 293 K.
- The upper boundary nodes did not consider any conduction terms, as it is assumed that the laser heating term dominates. This also removes any heat loss to the surroundings from the upper surface.

The material and laser constants used for the model are based on those used in a parallel experiment to validate the model. These can be found in **Appendix B** and are taken from [6]. To capture the behaviour of the system accurately the behaviour of the nodes at melting and evaporation temperatures must be modified. Using logical if statements in the code, when a node reaches sufficient temperature to melt the following correction is applied. (Eq.6)

$$T_{new} = T_{old} - \frac{Lm}{Cp} \quad \text{Eq. 6}$$

When a node reaches the evaporation temperature, the node is permanently fixed to the melting temperature of the material to simulate the loss of energy from the material during evaporation. Hence the cooling effect of evaporation is included in the model. Also, the ablated nodes are ignored in subsequent timesteps, so that the laser penetrates the material. This was done by taking the depth of ablation from the previous time step and altering the depth in the z-direction for nodes in the current time step. If the three nodes directly above were ablated, then the fourth node was set

to have a z-depth that would make it a surface node and the fifth node would have its depth changed to that of a node just below the surface and so on etc. This was implemented in each column of nodes. The model was formulated around a MATLAB function that calculates the matrix containing the temperature value of each node based on the previous temperature matrix. Firstly, various laser and material data were inputted/calculated. Then using the mesh selected the depth and position information of each node was initialised. This was then inputted to the function with the structure shown in the flowchart shown in **Figure 1**.

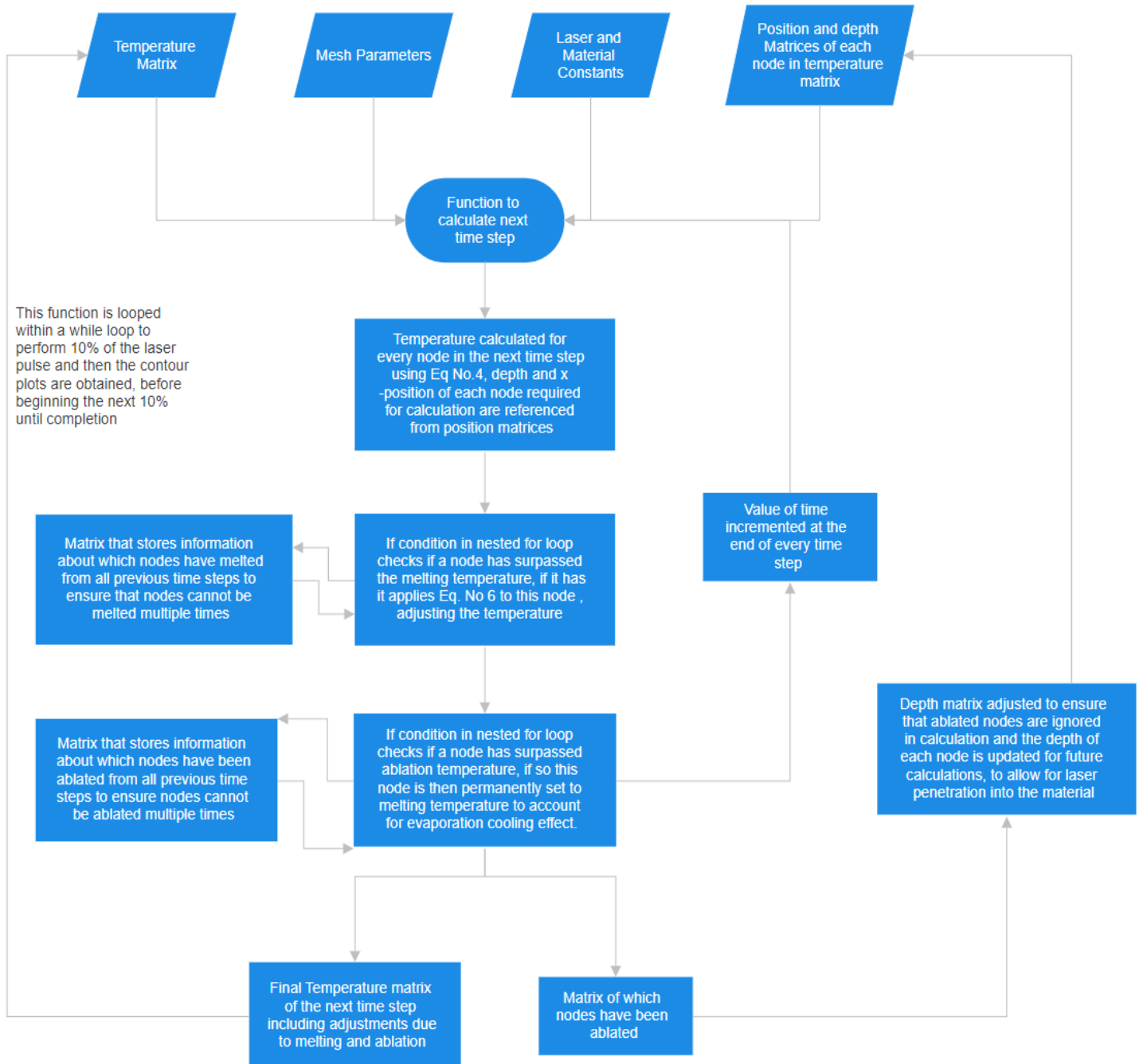


Figure 1- Flowchart showcasing the structure of the created MATLAB function that calculates the matrix containing the next time step temperature values. See **APPENDIX D**

## Results

Firstly, the most effective mesh to use for determination of results was investigated. The following meshes with x and z increments as given in **Table 2** were used:

Table 2- Different Mesh Sizes Investigated

Mesh Number	dx ( $\mu\text{m}$ )	dz ( $\mu\text{m}$ )
1	2	0.4
2	1	0.2
3	0.5	0.1
4	0.25	0.05
5	0.125	0.025

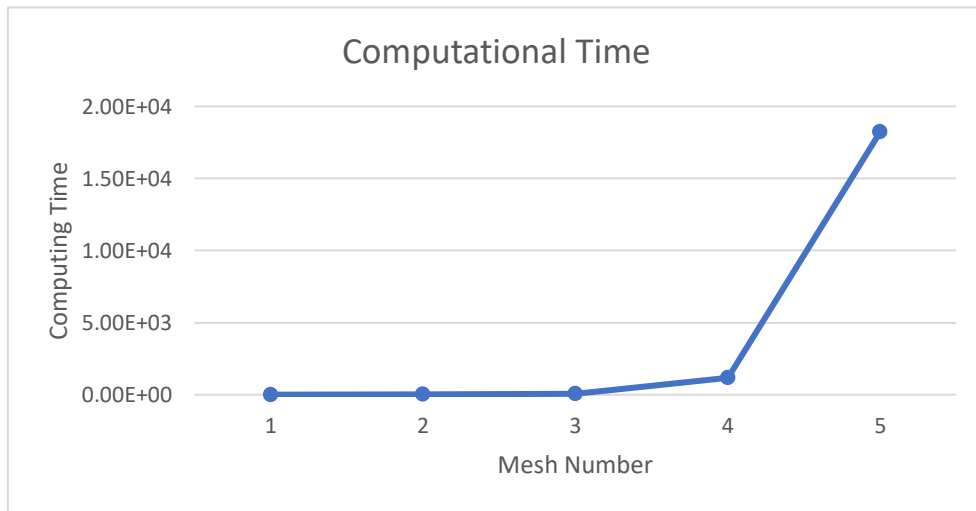


Figure 2- Mesh Number Vs Computational Time

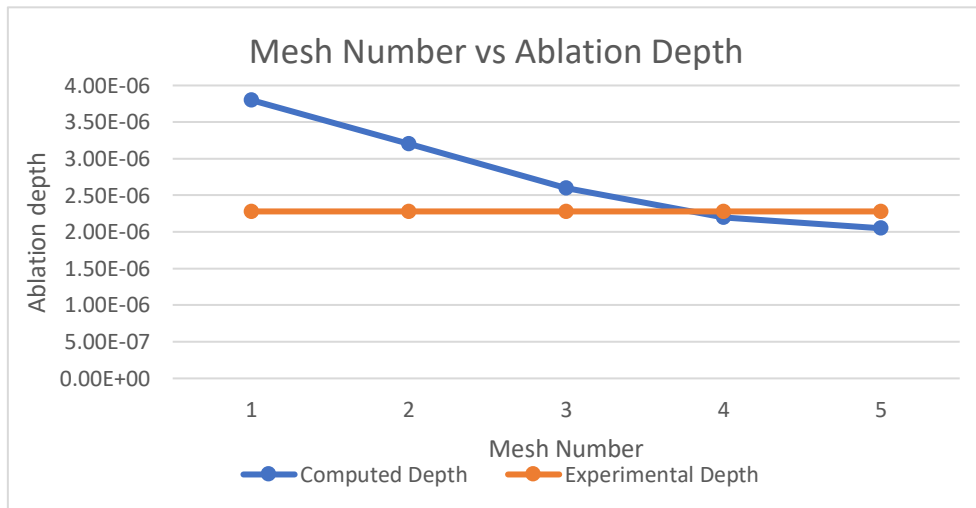


Figure 3- Different maximum Ablation depth of different Meshes.

Mesh number 3 was chosen as it was the quickest computational time (89 s) that was within 20% of the experimental validation. With a computed maximum ablation depth of **2.6 microns**, the experimental result being a depth of **2.28 microns**. This 14% difference is acceptable accuracy to validate the model. With this selected mesh size, the following contour plots of ablation front and melt front depth were obtained. Additionally, the comparison of different laser average powers and the effect this has on the final ablated crater depth was also investigated. See **Appendix A** for the temperature distribution contour plots.

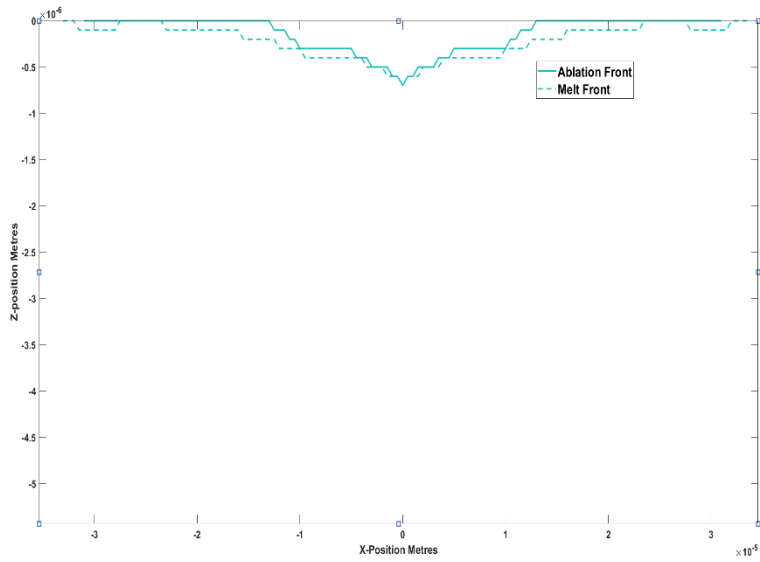


Figure 4-Contour plot of Ablation and Melt depth at 10% of laser Pulse

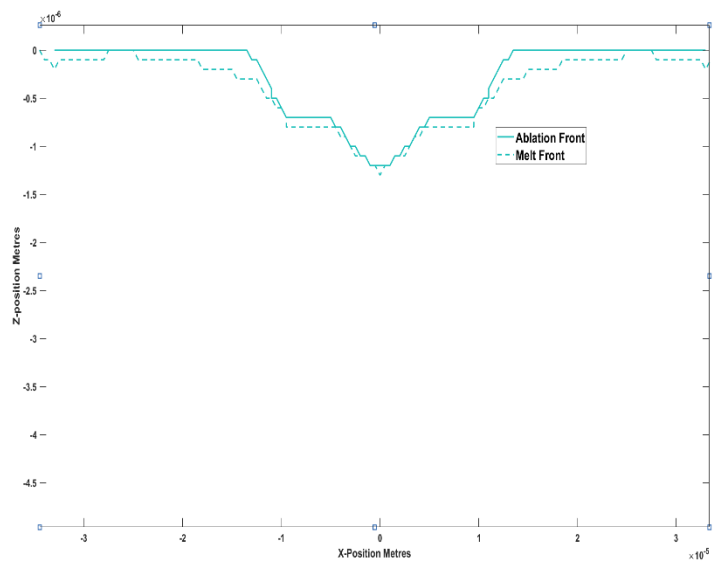


Figure 5-Contour plot of Ablation and Melt depth at 20% of laser Pulse

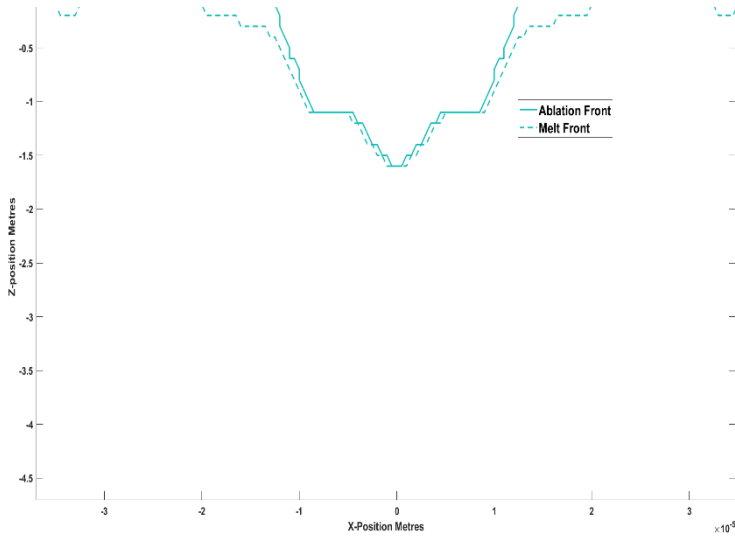


Figure 6-Contour plot of Ablation and Melt depth at 30% of Laser Pulse

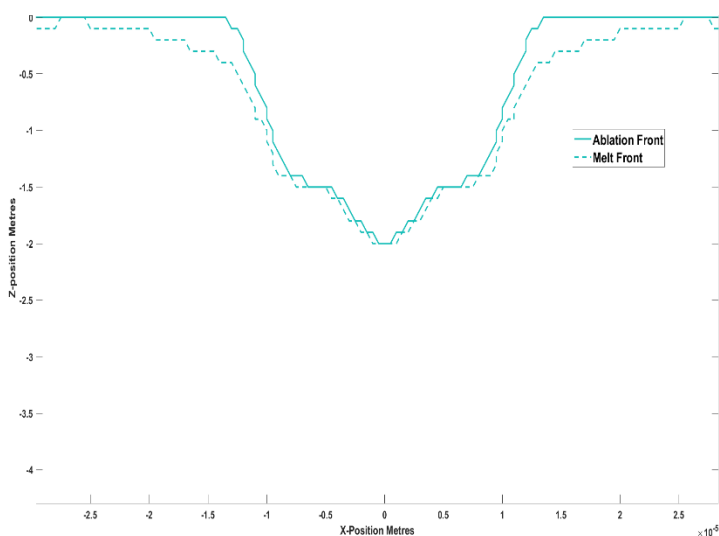


Figure 7-Contour plot of Ablation and Melt depth at 40% of Laser Pulse

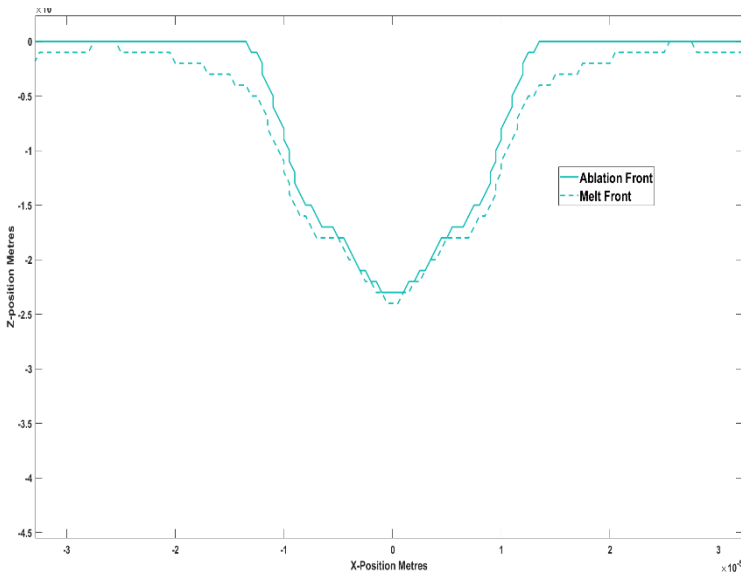


Figure 8-Contour plot of Ablation and Melt depth at 50% of Laser Pulse

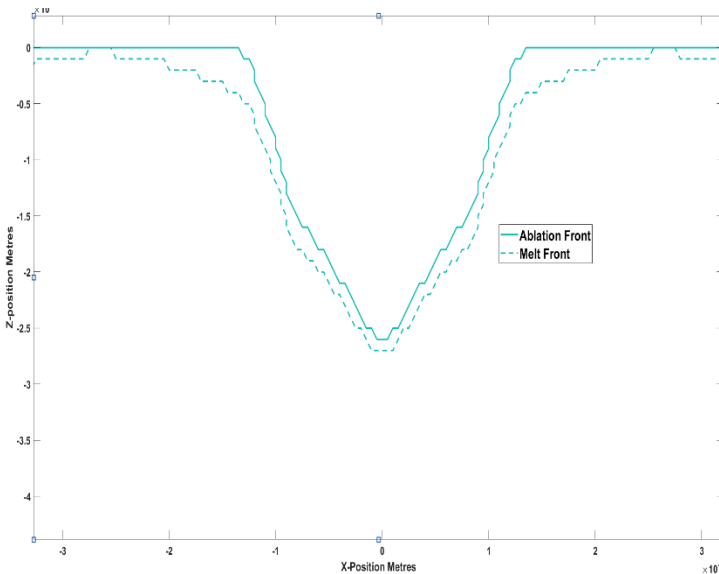


Figure 9-Contour plot of Ablation and Melt depth at 60% of Laser Pulse

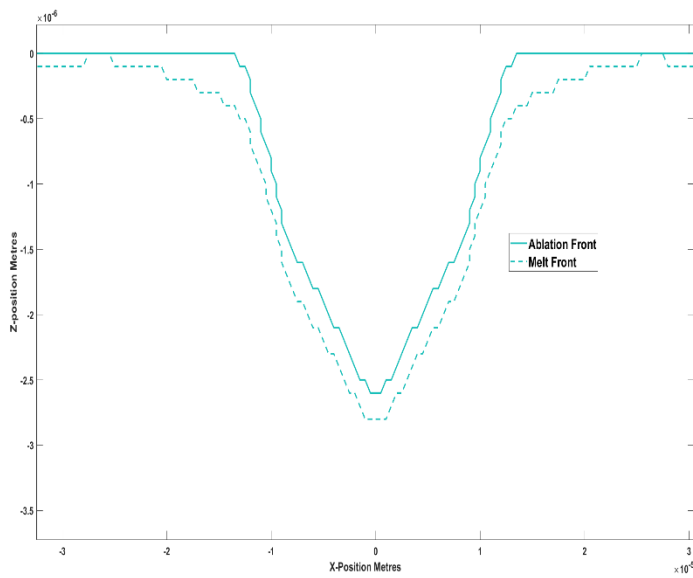


Figure 10- Contour plot of Ablation and Melt depth at 70% of Laser Pulse

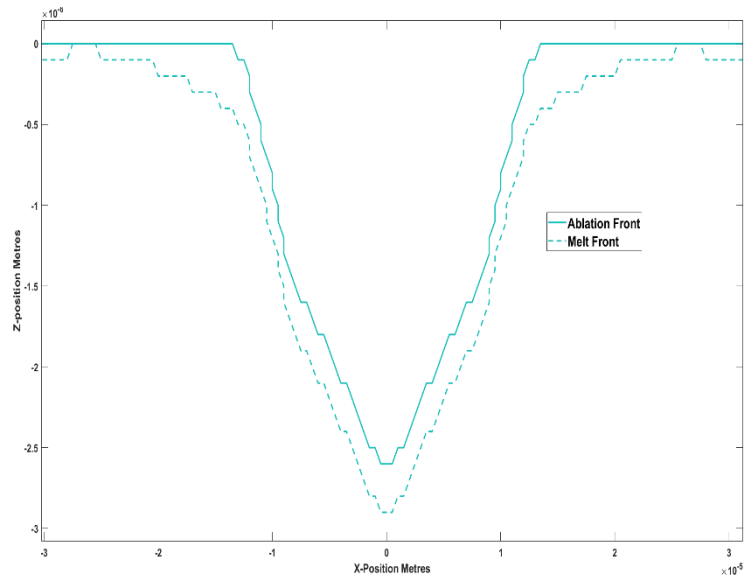


Figure 11-Contour plot of Ablation and Melt depth at 80% of Laser Pulse

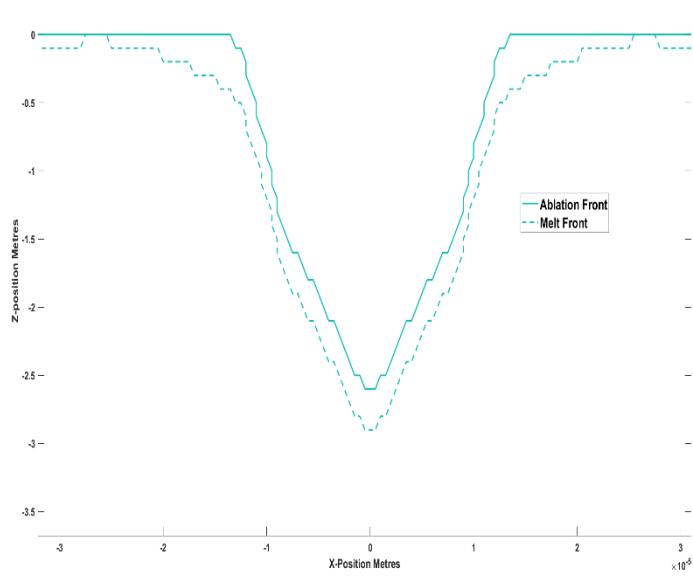


Figure 12-Contour plot of Ablation and Melt depth at 90% of Laser Pulse

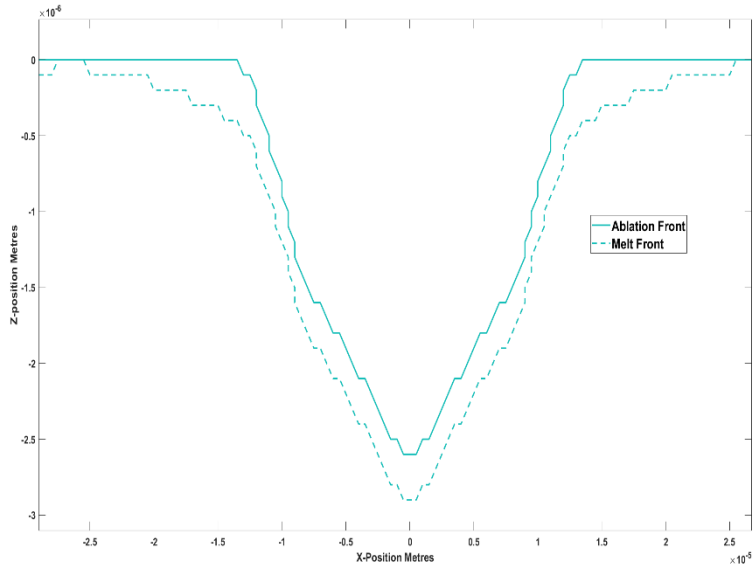


Figure 13-Contour plot of Ablation and Melt depth at 100% of Laser Pulse

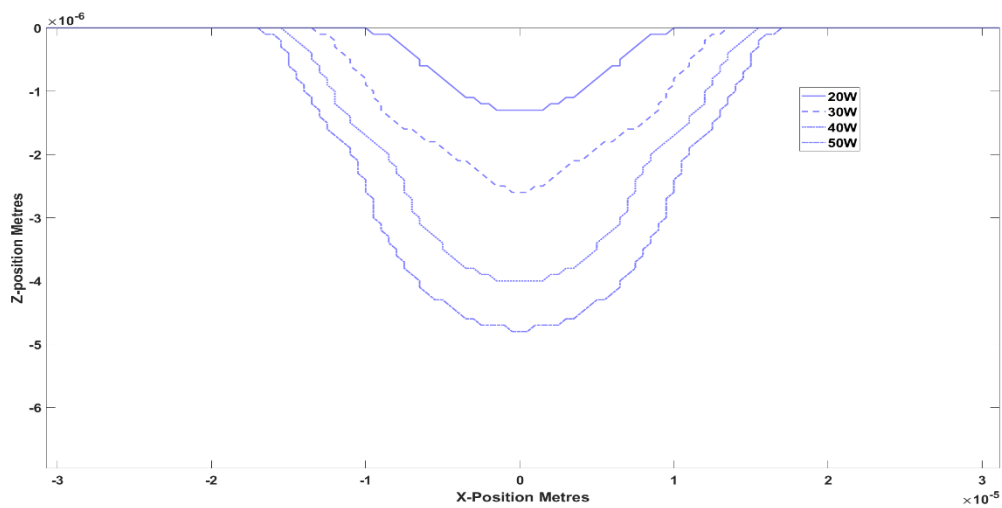


Figure 14-Contour plot of ablated craters at different Laser average power

## Discussion

It can be seen from the ablation contour plots that the crater formation is approximately gaussian, this is to be expected when using a Gaussian function as the volumetric heat source. The gaussian distribution in the X-direction ensures that the nodes at the centre of the laser beam spot are more readily ablated. Hence, the laser penetrates into the central nodes more rapidly than towards the edges. This leads to the gaussian distribution. This is in coherence with the distribution observed in a study using this approach for microsecond laser range pulses. [6]

The box like appearance of certain fronts on the ablation and melt fronts is due to the mesh. The material is depicted as a sequence of discrete nodes, there is no shape function [7] to interpolate between the nodes. For clarification, a node is either ablated or not ablated so the matrix that represents the depth of ablation is binary, giving the boxlike appearance of the front. This could be amended with a finer mesh or perhaps a finite element approach.

It is also an important observation to regard the growth of the ablation and melt front. Initially, they are almost identical except for close to the surface. This continues until 50% of the laser pulse (**Figure 8**), the ablation front then grows more slowly than the melt front until 70% of the laser pulse (**Figure 10**) where the ablation front reaches its maximum depth of **2.6 microns**. Then the melt front begins to grow at a decreasing rate for the rest of the simulation, reaching a final depth of **2.9 microns** (**Figure 13**). This behaviour is linked to the mathematical representation of the temporal energy distribution of the laser pulse. After 50% of the pulse the energy delivered to the substrate by the laser heating term is diminishing due to the gaussian function. Hence after 70% there is insufficient energy (Threshold energy) delivered to ablate any further material [8] through the melted layer. However, some energy is still delivered to, or already present in, the nodes just after the ablation front. Which for the remainder of the simulation causes the growth of the melt front in all directions via conduction between the nodes.

At first the laser heating dominates, leading to rapid ablation and a very small melt layer. Then as the laser heating decreases past the simulation midpoint due to the tail of the gaussian temporal energy distribution, the ablation and melt front begin to separate due to conduction in the material becoming more significant than the laser heating term. This is seen in the uniform growth away from the ablation layer of the melt layer past 70% in the simulation. This domination by the conduction term is always visible at the edges of the beam spot radius due to the spatial gaussian function, which explains the thicker melt layer and minimal ablation in these regions.

The recast layer can be considered the difference between the melt front and the ablation front. The recast layer thickness provides information about the depth of microstructural refinement caused by the phase change and rapid cooling. [9] Laser melting can change the grain structure to austenitic structure,[10] improving hardness. [11] also showed the induction of various crystal structures on carbon fibre. Therefore, the depth of such crystallisation can be studied with this approach. The recast layer thickness varies from **0.2 microns to 0.4 microns** across the simulated distribution.

To further this, the depth of the heat affected zone could [12] also be investigated by this method. The HAZ can have enhanced energy absorption characteristics associated with the large amount of austenite grains and small amounts of ferrite grains [13]. Material parameters could be readily implemented into this tool and the temperature distribution used to estimate the depth of microstructure refinement caused by the thermal processing. This has applications in many areas where the microstructure of a material is very important, such as promoting osteointegration in dental implants [14].



For an increase in average laser power, the depth of ablation is increased as shown in **(Figure 14)**. The width of the crater is also increased although this approaches a limit at the boundaries of the laser spot size as it is limited by the spatial gaussian distribution. Hence, material removal rate is increased with an increase in laser average power. Identical behaviour to that observed in [6].

The temperature distributions plots in **Appendix A** show that the heat can penetrate to a greater degree than just the melt front. Temperatures of **800 K** reach up to **3.8 microns** deep into the material. Hence heat transfer into the material by conduction is present. Therefore, thermal processing defects such as microcracks [15] should be anticipated. This model could be used to pre-empt the depth of these defects in different materials.

The temperature plots seen in **Appendix A** demonstrate the formation of locally heated regions in a symmetrical pattern near the surface of the material **(Figure 24)**, at regions not affected by the laser heating as they rest out of the radius of the beam spot, this does not occur in experimental studies [6]. These features are errors and are associated with the simulation boundary conditions. As the surface nodes do not have conduction modelled, these localised 'pockets' form as the heat cannot be conducted away from the surface but must go inwards.

However, due to the coherence between the experimental and simulated ablation depths, it can be reasoned that these localised heat pockets do not affect solution ablation accuracy. They are merely the result of the simplifications made about the heat interaction at the surface of the material. To obtain a more accurate temperature distribution contour plot, a more detailed simulation including convection and the generation of the plasma plume of ablated material [16] should be made.

There is also a distinct lack of a gaussian shape in the experimentally produced contour of the ablated depth as seen in **Appendix C**. It is more bowl like compared to simulation results. The simulation assumes a diffraction limited laser with  $M^2 = 1$ . Whereas in reality the laser quality suffers from errors such as but not limited to aberration. [17] In the simulation the results are taken instantaneously. However, from the experimental procedure the results are made after the substrate has been transferred to the microscope. This means that the flow of melted substrate and plasma [18] could act to fill in this gaussian distribution. This behaviour could 'dampen' the appearance of the gaussian crater by causing melted substrate to 'fill in' the curve. Leading to the discrepancy between the experimental and simulated distributions.

## Conclusion

- The Model achieved an ablated crater depth of **2.6 microns**. Within **14 %** of experimental result. **(2.28 microns)** Showcasing the suitability of the Finite difference method.
- The simulated crater had a gaussian shape, which was not seen in experimental validation, potentially due to translation of molten material.
- Material removal rate is increased by increasing laser average power.
- The ablation maximum depth is complete by **70%** of the laser pulse, however melting occurs for the entire duration of the laser pulse. Laser heating dominates initially, then conduction heat transfer as the laser pulse reaches its end.
- The assumptions about surface thermal interactions used are insufficient to determine an accurate temperature distribution, more complex models involving the convection and plasma interaction should be developed for further investigation.
- The recast layer has an average thickness of **0.3 microns**, and temperatures of up to **800 K** penetrate up to **3.8 microns** deep into stainless steel 316. This constitutes the heat affected zone.

## APPENDIX A: Temperature Contour Plots

Temperature contour plots are kept in the appendix to ensure adequate viewability:

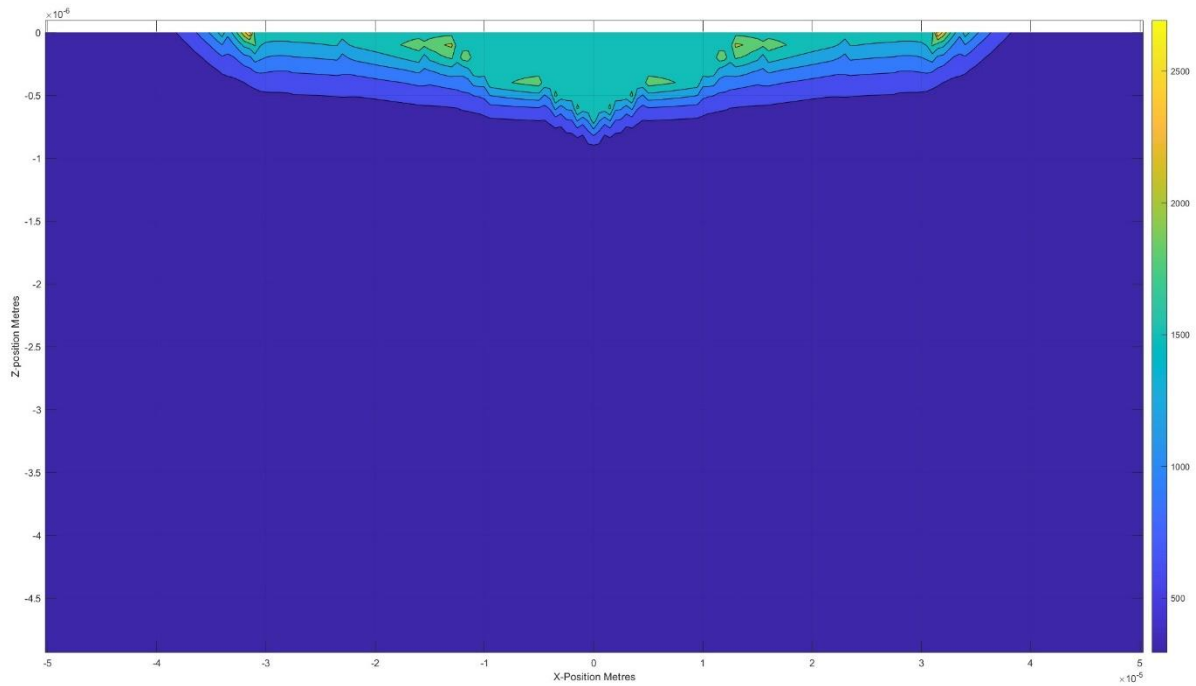


Figure 15- Temperature contour plot at 10% of laser Pulse

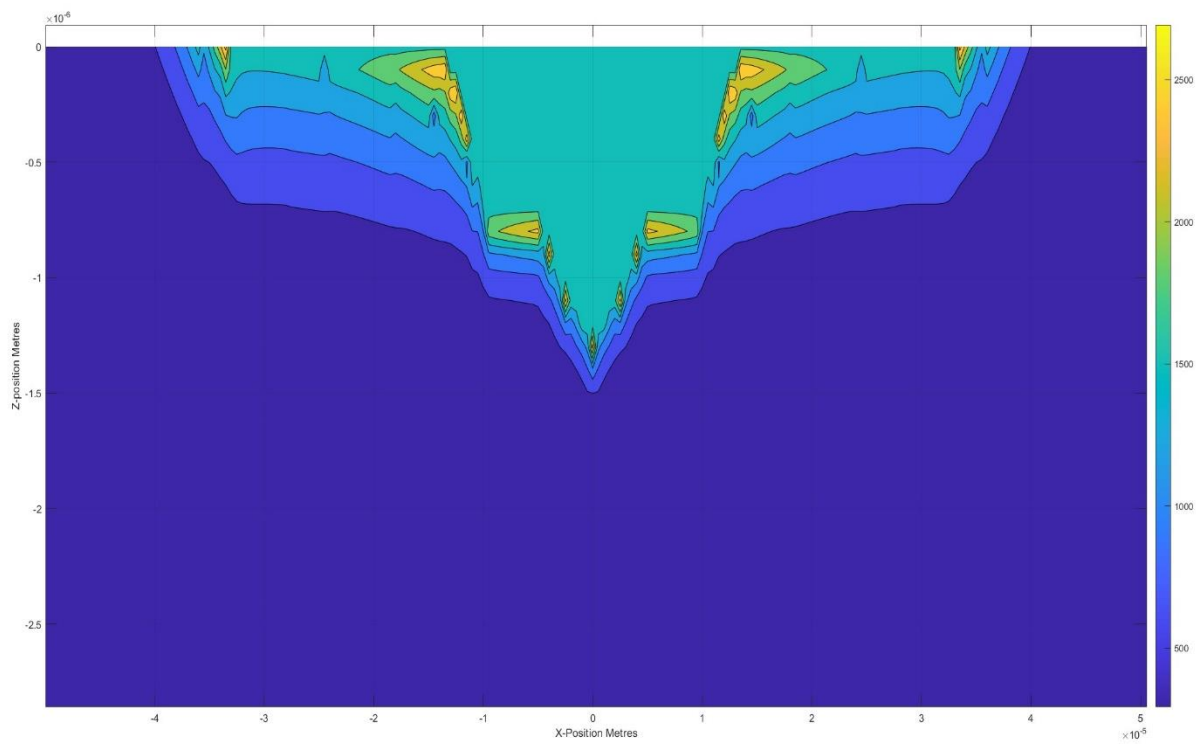


Figure 16- Temperature contour plot at 20% of laser Pulse

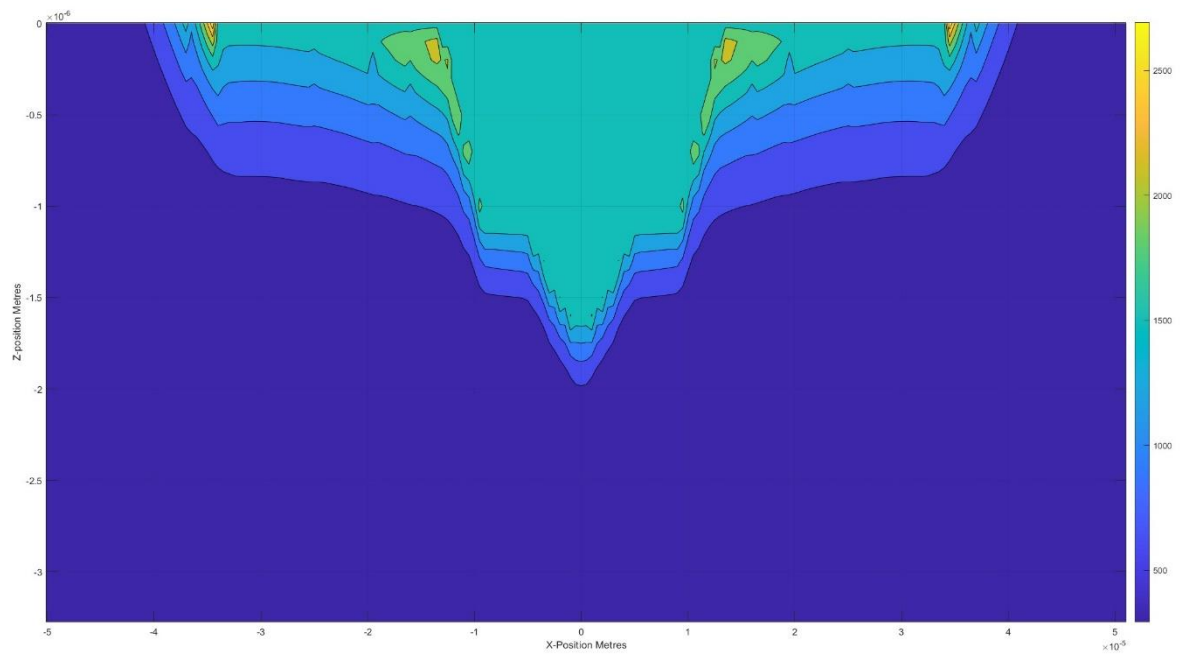


Figure 17- Temperature contour plot at 30% of laser Pulse

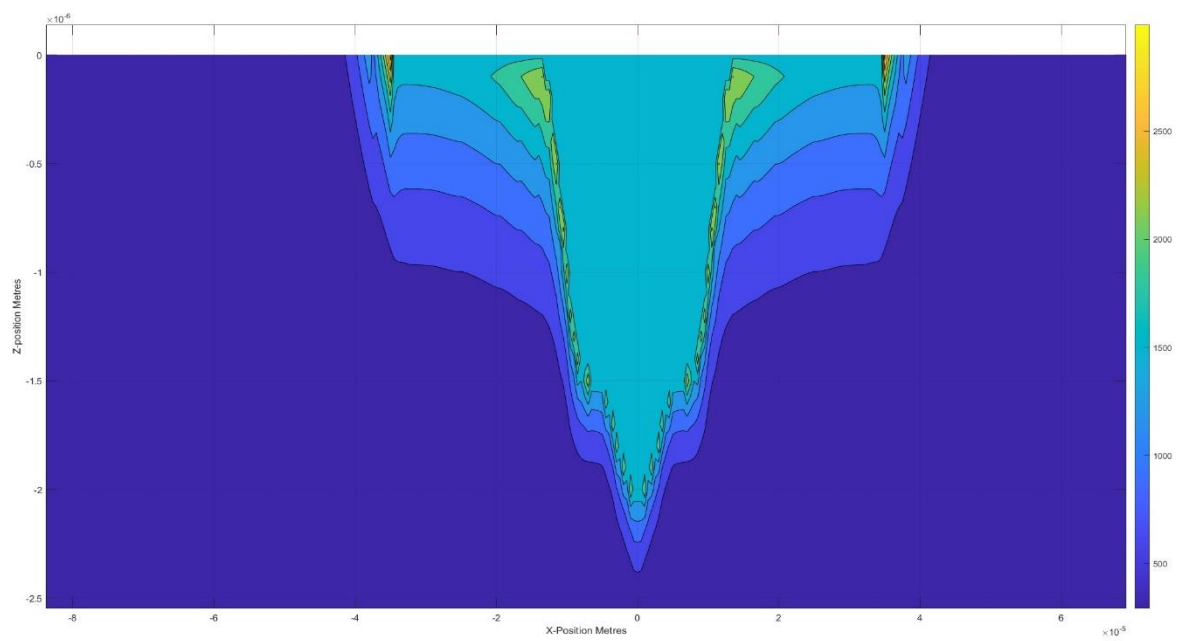


Figure 18- Temperature contour plot at 40% of laser Pulse

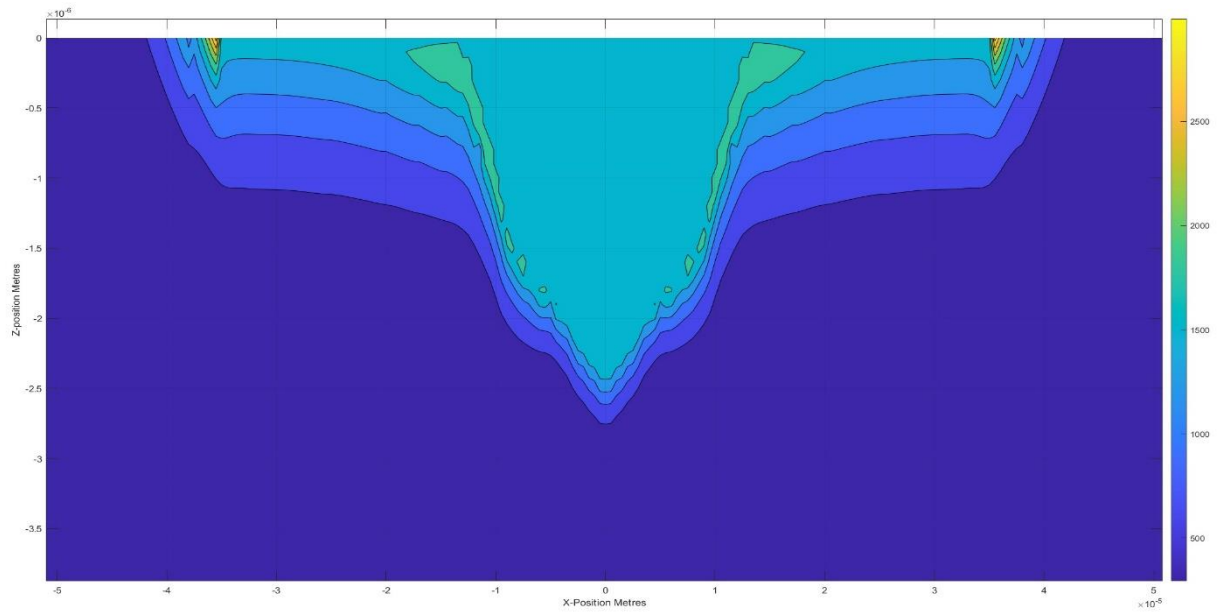


Figure 19- Temperature contour plot at 50% of laser Pulse

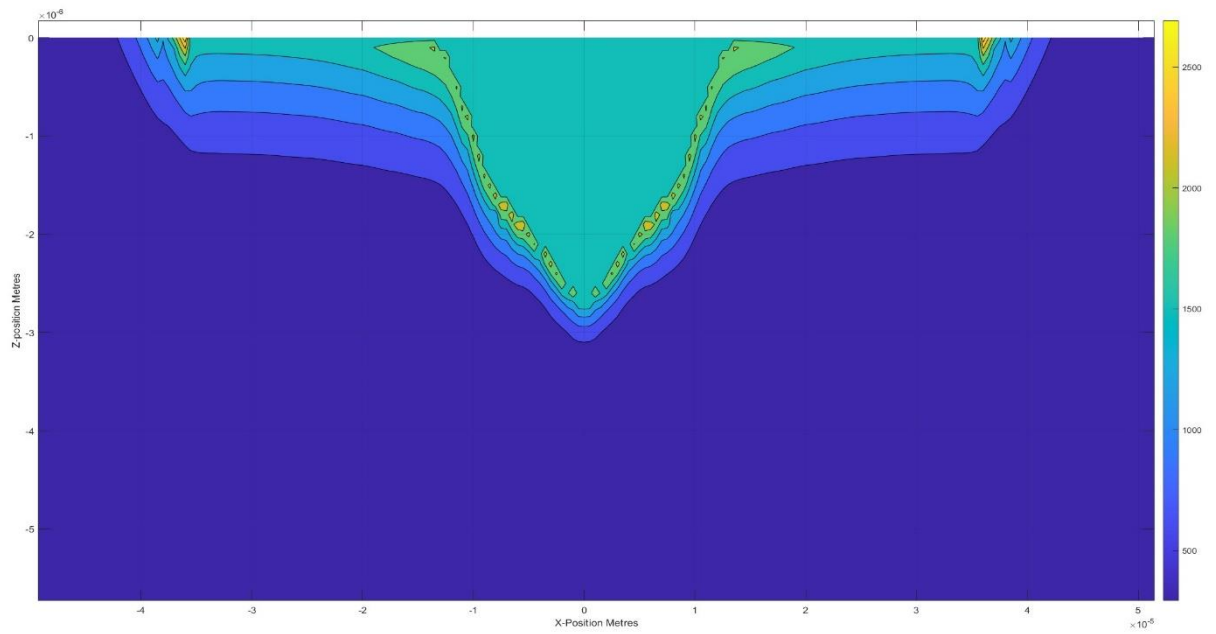


Figure 20- Temperature contour plot at 60% of laser Pulse

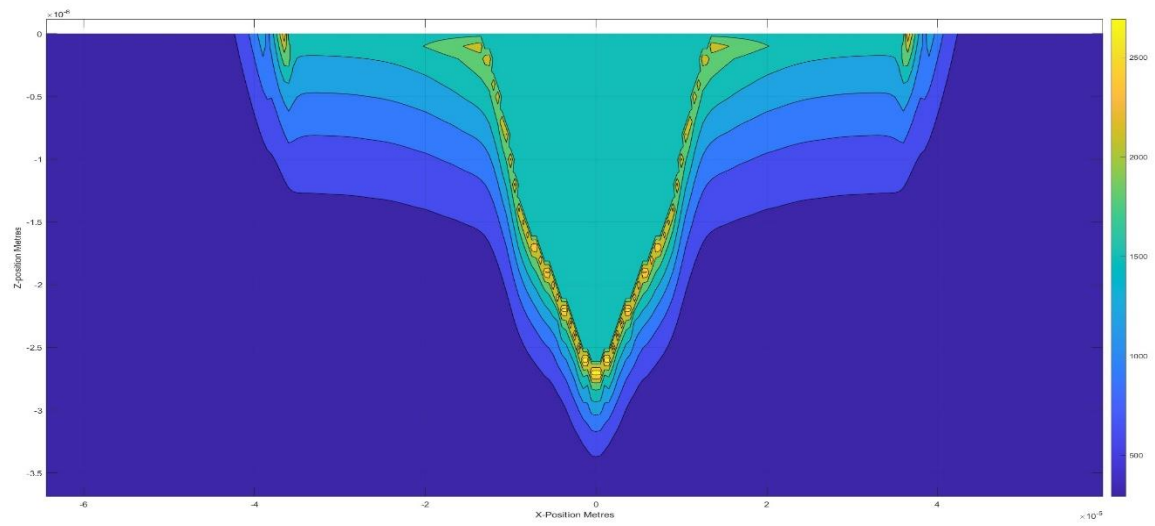


Figure 21- Temperature contour plot at 70% of laser Pulse

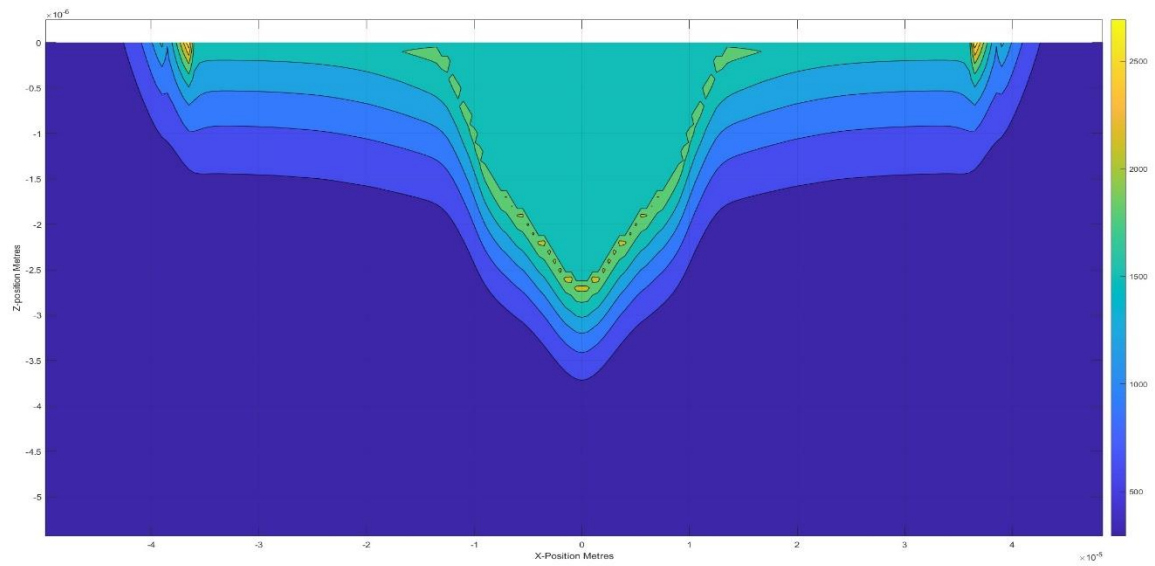


Figure 22- Temperature contour plot at 80% of laser Pulse

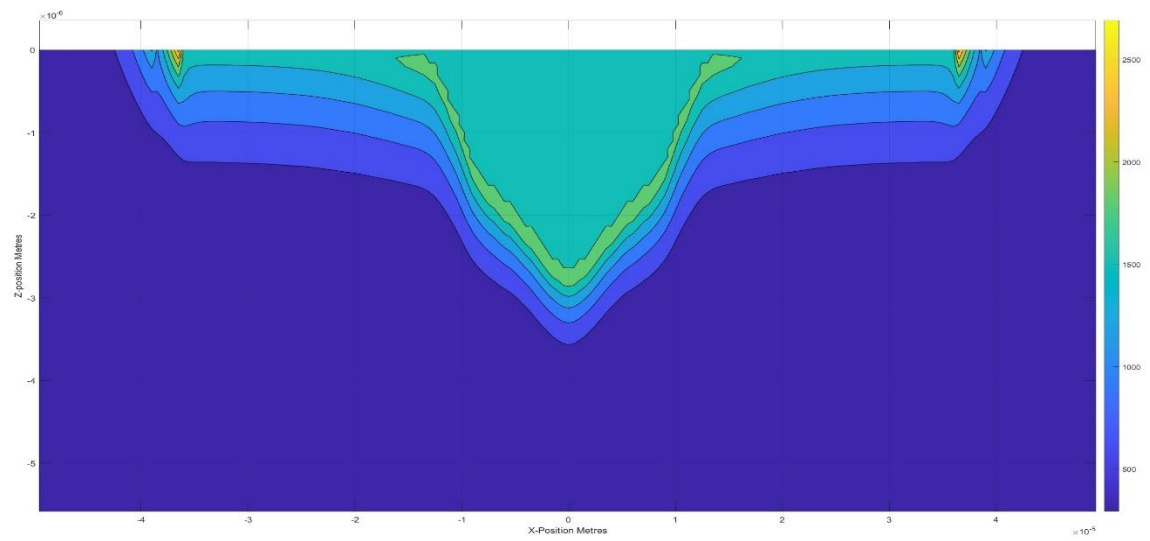


Figure 23- Temperature contour plot at 90% of laser Pulse

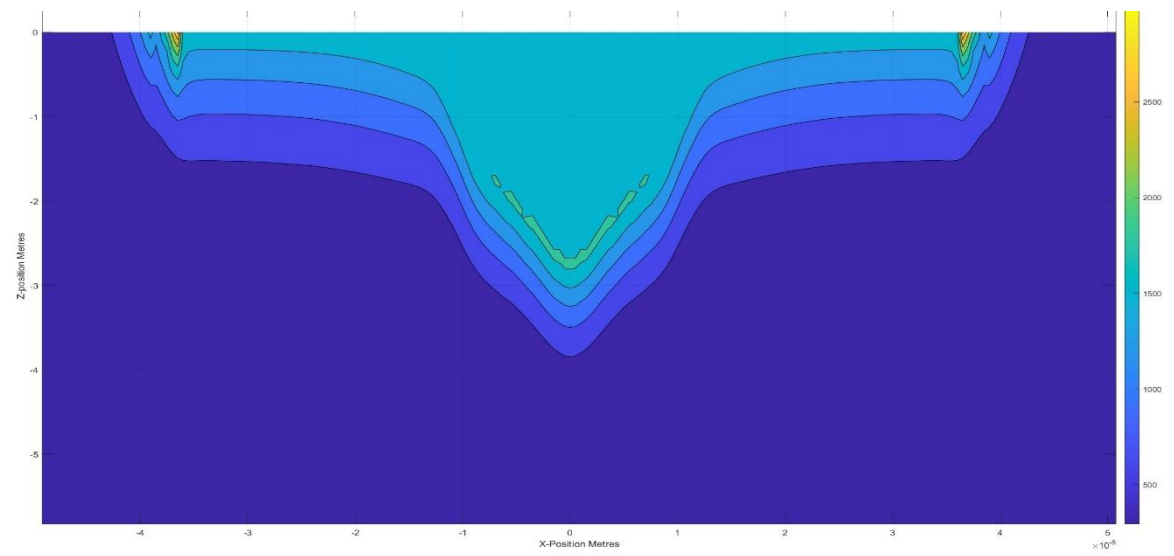


Figure 24- Temperature contour plot at 100% of laser Pulse

## Appendix B: Material and Laser Constants

Table-3 Material Constants and Laser parameters used for the simulation.

Absorption co-efficient( $m^{-1}$ )	$5.45 * 10^7$
Density( $\frac{kg}{m^3}$ )	8238
Specific Heat capacity( $\frac{J}{kgK}$ )	468
Thermal conductivity( $\frac{W}{mK}$ )	13.4
Evaporation Temperature(K)	3173
Melting Temperature(K)	1670
Latent Heat of melting( $\frac{kJ}{kg}$ )	300
Repetition Frequency(kHz)	70
Pulse Duration(ns)	220
Average Laser Power(W)	30
Beam Spot Radius ( $\mu m$ )	20

## Appendix C: Experimental Results

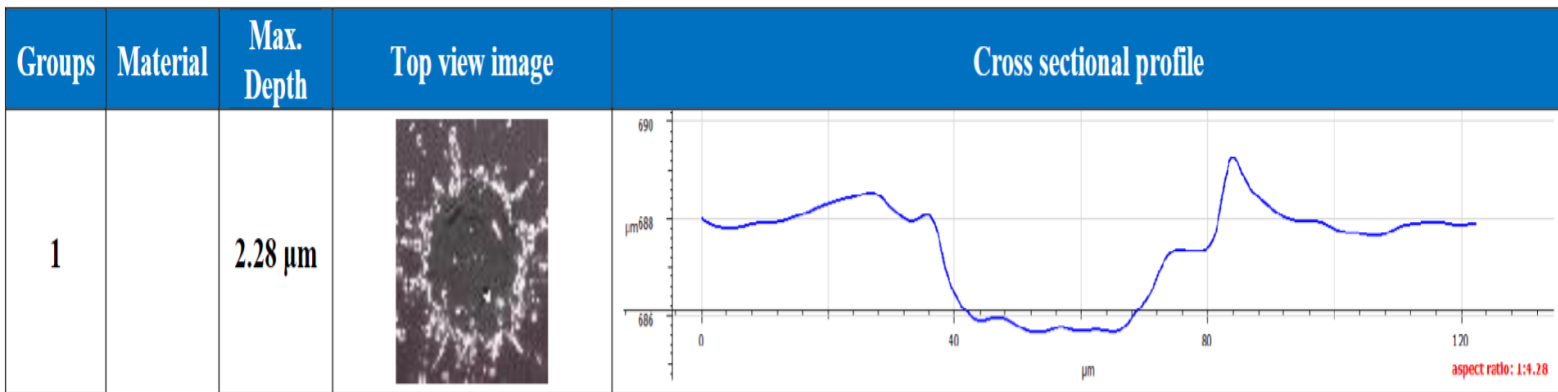


Figure 25- Ablation Contour plot from experiment for specified laser parameters given in **APPENDIX B**.

# Appendix D: MATLAB Code

```

1  format short
2  tic
3  %Setting up the the mesh size
4  dx=0.5*10^-6
5  dz=0.1*10^-6
6
7  %Material Properties Density, Specific heat capacity and thermal
8  %conductivity
9  Rho=8238
10 Cp=468
11 K=13.4
12 alpha=K/(Rho*Cp)
13
14 %Setting up the laser intensity parameters to be used in the FDM code
15 Pav=20
16 freq=70*10^3
17 tau=220*10^-9
18 Radius=20*10^-6
19 area=pi*Radius^2
20 LaserProp=Pav/(freq*tau*area)
21
22
23 %Setting up the row vector containing the x distance of each row element in
24 %the temperature matrix, in both positive and negative directions
25 Ineg=(-200*10^-6:dx:200*10^-6)
26 %Setting up the row vector with the z position information for each node
27 Zd=(0:dz:80*10^-6)
28 Zpos= repmat(Zd',1,length(Ineg))
29 %Setting up the matrix of initial temperatures
30 Initial=ones(height(Zpos),length(Ineg)).*293;
31 %calculating the time step recommendation
32 dt=0.5*(Rho*Cp*(dx^2)*(dz^2))/(K*(dx^2+dz^2))
33
34 %Time Step Control
35 dt=dt/10
36 %Setting up the initial function inputs
37

```

Command Window

```

>>
fx >>

```

```

45
46 %10%
47 g=1;
48 while time < tau*0.1
49     Zd=(0:dz:80*10^-6);
50     Zpos= repmat(Zd',1,length(Ineg));
51
52     if g/21==floor(g/21)
53         %Calling the function to calculate the next time step temperature matrix
54         [d,CorrMatrix,DepthMatrix]=LaserFDM(d,dx,dz,dt,alpha,LaserProp,Ineg,Zpos,time,CorrMatrix,DepthMatrix);
55     else
56         [d,CorrMatrix,DepthMatrix]=LaserFDM1(d,dx,dz,dt,alpha,LaserProp,Ineg,Zpos,time,CorrMatrix,DepthMatrix);
57     end
58     %Incrementing time
59     time=time+dt;
60     g=g+1;
61
62 end
63 CorrMatrix;
64 DepthMatrix;
65
66 %Code here to calculate contour plots with adequate temperature range
67 contourf(Ineg,-Zd,d,[293:300:3143])
68 colormap('parula')
69 xlabel('X-Position Metres')
70 ylabel('Z-Position Metres')
71 grid on
72 colorbar
73 contour(Ineg,-Zd,DepthMatrix,[1 1],'LineStyle','-','LineWidth',2)
74 colormap('parula')
75 hold on
76 contour(Ineg,-Zd,CorrMatrix,[1 1],'LineStyle','--','LineWidth',2)
77 xlabel('X-Position Metres')
78 ylabel('Z-position Metres')
79 legend('Ablation Front','Melt Front')
80
81 hold off
82

```

Command Window

```

>>
fx >>

```



### Function Described in Figure 1:

```
function
[NextTimeStep,CorrMatrix,DepthMatrix]=LaserFDM(A,dx,dz,dt,alpha,LaserProp,Ineg
,Zpos,time,CorrMatrix,DepthMatrix)
%additional parameters needed for calculation of laser properties
Radius=(20*10^-6);%Radius of beam
tau=(220*10^-9);%Duration of laser Pulse
a=5.45*10^7;%Extinction co-efficient
B=(dt*a*LaserProp)*2.5970e-07;%Factor to multiply the laser heating function
by
%Set up first layer
j=1;
%Initialise next time step matrix
NextTimeStep=zeros(height(A),length(A));
%Recalculate the Zpos vector based on depth of vapourisation from previous
%time step
Depth=sum(DepthMatrix);
k=Depth.*dz;
p=Zpos-k;
Zpos=max(p,0);

%Loop for the top layer of nodes with BC
for i=1:(length(A)-1)
    Q=exp(-2*(Ineg(:,i)/Radius)^2);%X-direction Gaussian dist term
    M=exp(-2*(time/tau)^2);%Temporal gaussian dist term
    G=exp(-a*Zpos(j,i));%Z-direction term

    NextTimeStep(j,i)=A(j,i)+(B*Q*M*G);
end

%Nested loop to calculate the middle layers of the next time step
for j=2:(height(A)-2)
    for i=1:(length(A)-1)
        Q=exp(-2*(Ineg(:,i)/Radius)^2);
        M=exp(-2*(time/tau)^2);
        G=exp(-a*Zpos(j,i));
        if i==1
            NextTimeStep(j,i)=A(j,i)+((dt*alpha)*(((A(j,i+1)-
2*A(j,i)+293)/(dx^2))+((A(j+1,i)-2*A(j,i)+A(j-1,i))/(dz^2))))+(B*Q*M*G);
        elseif i==(length(A)-1)
            NextTimeStep(j,i)=A(j,i)+((dt*alpha)*(((293-2*A(j,i)+A(j,i-
1))/(dx^2))+((A(j+1,i)-2*A(j,i)+A(j-1,i))/(dz^2))))+(B*Q*M*G);
        else
            NextTimeStep(j,i)=A(j,i)+((dt*alpha)*(((A(j,i+1)-2*A(j,i)+A(j,i-
1))/(dx^2))+((A(j+1,i)-2*A(j,i)+A(j-1,i))/(dz^2))))+(B*Q*M*G);
        end
    end
end
```

```

        end
    end

    %Loop to calculate the bottom layer with BC
    j=(height(A)-1);
    for i=1:(length(A)-1)
        Q=exp(-2*(Ineg(:,i)/Radius)^2);
        M=exp(-2*(time/tau)^2);
        G=exp(-a*Zpos(j,i));
        if i==1
            NextTimeStep(j,i)=A(j,i)+((dt*alpha)*(((A(j,i+1)-
2*A(j,i)+293)/(dx^2))+((293-2*A(j,i)+A(j-1,i))/(dz^2))))+(B*Q*M*G);
        elseif i==(length(A)-1)
            NextTimeStep(j,i)=A(j,i)+((dt*alpha)*(((293-2*A(j,i)+A(j,i-
1))/(dx^2))+((293-2*A(j,i)+A(j-1,i))/(dz^2))))+(B*Q*M*G);
        else
            NextTimeStep(j,i)=A(j,i)+((dt*alpha)*(((A(j,i+1)-2*A(j,i)+A(j,i-
1))/(dx^2))+((293-2*A(j,i)+A(j-1,i))/(dz^2))))+(B*Q*M*G);
        end
    end
    end
    %Loop that checks if a new node has been melted and if so, applies the
    %rule to account for the latent heat of melting at that node
    for y=1:height(A)
        for x=1:length(A)
            if NextTimeStep(y,x)>= 1670 && CorrMatrix(y,x)==0
                NextTimeStep(y,x)=NextTimeStep(y,x)-(300000/468);
                CorrMatrix(y,x)=1;
            end
        end
    end
    %The depth matrix to calculate which nodes have been ablated
    for y=1:height(A)
        for x=1:length(A)
            if NextTimeStep(y,x)>= 3173 && DepthMatrix(y,x)==0
                DepthMatrix(y,x)=1;
            end
        end
    end
    %Loop to limit the temperature of ablated nodes at the vapourisation
    %temp to account for exaggerated thermal effects from these nodes
    for y=1:height(A)
        for x=1:length(A)
            if DepthMatrix(y,x)==1
                NextTimeStep(y,x)=1670;
            end
        end
    end
end
end

```

## REFERENCES

- [1] C. K. Ma, L. Aguilar, M. Karim, M. Abdun Nafi, J. Ma, and M. P. Jahan, "Experimental investigation of nanosecond laser Machining of 3D printed carbon fiber reinforced polymer (CFRP) composite," *Manuf Lett*, vol. 35, pp. 399–409, 2023, doi: <https://doi.org/10.1016/j.mfglet.2023.08.077>.
- [2] S. A. Tyagi and M. M., "Additive manufacturing of titanium-based lattice structures for medical applications – A review," *Bioprinting*, vol. 30, p. e00267, 2023, doi: <https://doi.org/10.1016/j.bprint.2023.e00267>.
- [3] B. N. Chichkov, C. Momma, S. Nolte, F. von Alvensleben, and A. Tünnermann, "Femtosecond, picosecond and nanosecond laser ablation of solids," *Applied Physics A*, vol. 63, no. 2, pp. 109–115, 1996, doi: 10.1007/BF01567637.
- [4] G. Anstett, M. Nittmann, A. Borsutzky, and R. Wallenstein, "Experimental investigation and numerical simulation of the spatio-temporal dynamics of nanosecond pulses in Q-switched Nd:YAG lasers," *Applied Physics B*, vol. 76, no. 8, pp. 833–838, 2003, doi: 10.1007/s00340-003-1189-4.
- [5] G. E. Jellison Jr. and D. H. Lowndes, "Optical absorption coefficient of silicon at 1.152  $\mu$  at elevated temperatures," *Appl Phys Lett*, vol. 41, no. 7, pp. 594–596, Oct. 1982, doi: 10.1063/1.93621.
- [6] T. Dobrev, S. S. Dimov, and A. J. Thomas, "Laser milling: Modelling crater and surface formation," *Proc Inst Mech Eng C J Mech Eng Sci*, vol. 220, no. 11, pp. 1685–1696, Nov. 2006, doi: 10.1243/09544062JMES221.
- [7] Tomasz G. Zielinski, *Introduction to the Finite element Method*. 1992.
- [8] Y. Wang *et al.*, "Ablation threshold modelling and validation of metal Nanosecond laser processing," *Opt Commun*, vol. 523, p. 128608, 2022, doi: <https://doi.org/10.1016/j.optcom.2022.128608>.
- [9] Y. Wang *et al.*, "Morphology modelling and validation in nanosecond pulsed laser ablation of metallic materials," *Precis Eng*, vol. 79, pp. 34–42, 2023, doi: <https://doi.org/10.1016/j.precisioneng.2022.08.010>.
- [10] S. K. P. *et al.*, "State of art: Review on laser surface hardening of alloy metals," *Mater Today Proc*, 2023, doi: <https://doi.org/10.1016/j.matpr.2023.04.259>.
- [11] A. Bhaumik and J. Narayan, "Nano-to-micro diamond formation by nanosecond pulsed laser annealing," *J Appl Phys*, vol. 126, no. 12, p. 125307, Sep. 2019, doi: 10.1063/1.5118890.
- [12] R. Le Harzic *et al.*, "Comparison of heat-affected zones due to nanosecond and femtosecond laser pulses using transmission electronic microscopy," *Appl Phys Lett*, vol. 80, no. 21, pp. 3886–3888, May 2002, doi: 10.1063/1.1481195.
- [13] L. Fengde *et al.*, "Study of the microstructure and impact properties of the heat-affected zone of high nitrogen steel for laser-arc hybrid welding," *Mater Res Express*, vol. 6, no. 7, p. 076505, 2019, doi: 10.1088/2053-1591/ab11f7.
- [14] R. Saran, K. Ginjupalli, S. George, S. Chidangil, and U. V K, "LASER as a tool for surface modification of dental biomaterials: A review," *Heliyon*, vol. 9, p. e17457, Jun. 2023, doi: 10.1016/j.heliyon.2023.e17457.
- [15] H. Huang, Y. Qian, C. Wang, and J. Yan, "Laser induced micro-cracking of Zr-based metallic glass using 1011 W/m<sup>2</sup> nano-pulses," *Mater Today Commun*, vol. 25, p. 101554, 2020, doi: <https://doi.org/10.1016/j.mtcomm.2020.101554>.
- [16] S. Tan, M. Wang, J. Wu, Y. Zhang, and J. Li, "A Study on the Plasma Plume Expansion Dynamics of Nanosecond Laser Ablating Al/PTFE," *Energies (Basel)*, vol. 13, no. 13, 2020, doi: 10.3390/en13133321.
- [17] R. Paschotta, "Beam Quality," *RP Photonics Encyclopedia*. Dec. 29, 2023. doi: 10.61835/8mq.
- [18] D. Arntz, D. Petring, S. Stoyanov, N. Quiring, and R. Poprawe, "Quantitative study of melt flow dynamics inside laser cutting kerfs by in-situ high-speed video-diagnostics," *Procedia CIRP*, vol. 74, pp. 640–644, 2018, doi: <https://doi.org/10.1016/j.procir.2018.08.057>.